Available online at www.sciencedirect.com

SCIENCE DIRECT®

Medical Image Analysis 9 (2005) 133–143

MEDICAL IMAGE ANALYSIS

www.elsevier.com/locate/media

From arteriographies to computational flow in saccular aneurisms: the INRIA experience

J.-D. Boissonnat *, R. Chaine, P. Frey, G. Malandain, S. Salmon, E. Saltel, M. Thiriet

INRIA, ARC VITESV [1], B.P. 105, F-78153 Le Chesnay Cedex, France

Abstract

Saccular aneurisms illustrate usefulness and possible techniques of image-based modeling of flow in diseased vessels. Aneurism flow is investigated in order to estimate the rupture risk, assuming that the pressure is the major factor and that high-pressure zones are correlated to within-wall strong-stress concentrations. Computational flow is also aimed at providing additional arguments for the treatment strategy. Angiographies of aneurismal vessels of large and medium size are processed to provide three-dimensional reconstruction of the vessel region of interest. Different reconstruction techniques are used for a side and a terminal aneurisms. Reconstruction techniques may lead to different geometries especially with poor input data. The associated facetisation is improved to get a computation-adapted surface triangulation, after a treatment of vessel ends and mesh adaptation. Once the volumic mesh is obtained, the pulsatile flow of an incompressible Newtonian blood is computed using in vivo non-invasive flowmetry and the finite element method. High pressure zones are observed in the aneurism cavity. The pressure magnitude in the aneurism, the location and the size of high pressure zones depend mainly on the aneurism implantation on the vessel wall and its orientation with respect to the blood flux in the upstream vessel. The stronger the blood impacts on the aneurismal wall the higher the pressure. The state of the aneurism neck, where a high-pressure zone can occur, and the location of the aneurism, with an easy access or not, give arguments for the choice between coiling and surgical clipping. Mesh size and 3D reconstruction procedure affect the numerical results. Helpful qualitative data are provided rather than accurate quantitative results in the context of multimodeling.

Keywords: 3D reconstruction; Aneurism; Finite element method; Mesh adaptation; Pulsatile flow

Introduction

Large-artery diseases are frequent and major causes of death. Atheroma induces intrinsec lumen narrowings or stenoses on the one hand and lumen enlargements or fusiform aneurisms on the other hand. The stenosis causes reduction in blood supply to the perfused tissues. Both complications are often associated with thrombus formation and, then, bolus displacements. When blocked in a smaller artery, the boli stop the perfusion of a more or less large region of the irrigated organ whether the artery bore is more or less small. The illustrated pathology in the present work is given by saccular (pouch-like or balloon-like) bulging of the artery wall, which undergoes a plastic deformation. Saccular aneurisms can occur after an infection or a traumatism of the artery wall. Congenital aneurisms are mainly observed at the branching sites of the arteries afferent to and efferent from the Willis circle, an anastomotic network between the three main cerebral arteries, the two internal carotid arteries and the basilar trunk, and their branches. A mechanically-induced degeneration of the wall internal elastic lamina has been proposed as the initiating cause of congenital aneurisms with genetic predisposition (vessel-wall structure deficiency in a frequent

---

* Corresponding author. Tel.: +33 93 65 77 38.
E-mail address: jean-daniel.boissonnat@sophia.inria.fr (J.-D. Boissonnat).

[1] Cooperative Research Initiative.

1361-8415/$ - see front matter © 2004 Published by Elsevier B.V.
doi:10.1016/j.media.2004.11.004

familial context), the rheology of the cerebral arteries being different from the one of the other arteries. Because haemodynamic factors are involved in genesis and development of artery wall diseases such the aneurisms, numerical simulations of blood flow are useful for medical practice. In order to take into account the huge between-subject variability in vessel anatomy and in lesion shape, which affect the flow and thus the pressure field within the aneurism, the computational domains are based upon angiographies.

When the aneurism is diagnosed, the medical checkup of the lesion is performed. Usual diagnosis procedures, like X-ray computed tomography (CT) – nowadays multi-slice spiral or helical CT – or magnetic resonance angiography (MRA), provide: (i) the aneurism location; (ii) the shape and size of both the cavity and the neck; (iii) its implantation on the vessel wall; (iv) the situation and shape of neighbouring organs and vessels. The neck is defined as the channel between the artery and the wall dilation (Fig 1). The main region is called the cavity (or pouch or sac). Opposite to the neck is the dome (or fundus) of the aneurism. The cavity can be biloculated with a large lateral compartment, which is called below the nose (a projecting end part of the aneurism sac). The sac wall situated in front of the nose is called hereafter the nucha. Saccular aneurisms are classified into three categories according to its largest width (small, large – $12 \leqslant w_a \leqslant 25$ mm – and giant). The aneurism is located either on the vessel edge, and then called side aneurism, or at a branching region, and called lateral or terminal whether the vessel trunk (or stem) gives birth to a lateral branch or divides into two main daughter vessels. The orientation between the aneurism and the vascular stem, i.e., the angle between the greatest aneurismal length and the main-flow local direction, is an important criterion, which is associated with the lesion-growth time scale and with the complication risk estimation, as well as with the treatment planning.

Informations on the local blood flow and its impact on the aneurism wall give important parameters for the medical checkup. When the outpouching arises from the carina of a vessel bifurcation, it points in the direction taken by a significant part of the bloodstream whereas it is less irrigated when located on the edge of a curved vessel. Both tangential and normal blood stresses applied to the aneurismal wall have been considered to explain complications. Repetitive acute increases in shear stress at the blood–wall interface may damage the endothelium and induce the formation of thrombi. Congenital intracranial aneurisms are located at the branching apex where the pressure is locally high.

Compression of neighbouring vessels and embolic episodes belong to evolution risks. The vessel wall may become thinner and weaker than the normal artery wall. When the pressure is high enough to subject the wall to high stresses, wall rupture, the most dangerous complication, can occur. The larger the aneurism and/or the higher the intra-aneurismal pressure, the greater the probability of aneurism rupture. When a cerebral aneurism ruptures, it bleeds usually into the subarachnoid space within the skull. The subarachnoid haemorrhage can lead to a vasospasm which can induce death rather than the haemorrhage itself. On the contrary, ruptured aneurisms located in other soft parts of the body can lead to massive haemorrhage.

Two main therapies may be applied to saccular aneurisms. The first treatment consists in placing a small metallic clip across the base of the aneurism whereas the normal artery wall is reconstructed to maintain blood flow to the irrigated tissues. The endovascular treatment (interventional medicine) is an alternative to surgical clipping, especially when it is associated with a high complication risk. It is based on percutaneous, minimally invasive image-guided catheter-based procedures. The aneurism can be excluded with a stent, especially when the aneurism cavity is widely opened on the vascu-

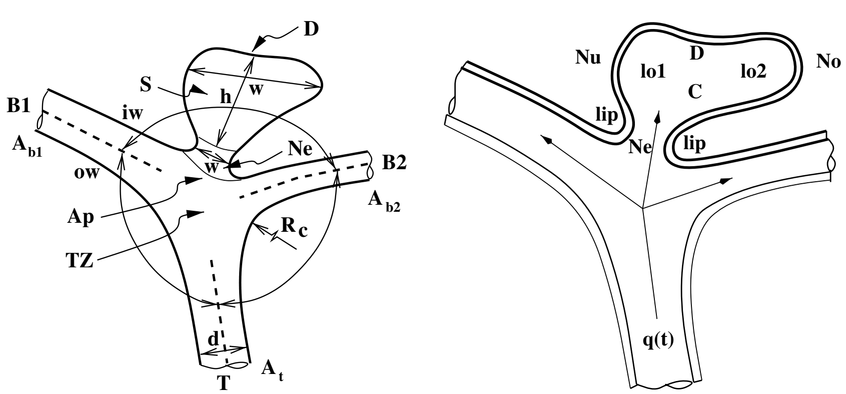

Fig. 1. Schematic drawing with geometry definitions of a saccular aneurism at the apex Ap of a branching segment of an artery: S, aneurism sac (or cavity C) of width w and height h; Ne, aneurism neck of width w; D, aneurism dome; T, trunk of hydraulic diameter d and cross-sectional area A_t; B, branch of cross-sectional area A_b; TZ, transition zone; ow and iw, outer and inner bend; α, β, θ: branching angles; R_c, local curvature radius. The aneurism sac is composed of two compartments or loculi lo1 and lo2. No: nose, Nu: nucha.

lar lumen. Besides, when a covered stent is employed, it must not induce any vessel obstruction. Otherwise, coiling is used. The aneurism cavity is filled with coils, which have a circular memory, in order to obtain a complete, stable exclusion of the lesion from the arterial circulation with preservation of the diseased vessels. This endovascular procedure is indeed difficult because wall rupture must be avoided. Aneurismal perforation during coiling may appear especially when the catheter tip location is fluctuating due the local flow pattern. Coils do not then necessarily enter in the whole aneurismal cavity during coiling. Moreover, coil compaction occurs, i.e., the coils are pushed toward the dome by the arterial flow. A residual cavity is thus often observed after coiling. The coiled part of the aneurism becomes acutely occluded with thrombi generated by the coils. Coils must not be located near the blood stream in order to avoid embolisms. From the residual cavity, recanalization can appear. Recanalization depends on the aneurism type in relation with the local blood flow. In particular, the sac and orifice sizes are important short-term prognosis factors because they affect the occlusion quality.

Nowadays, scanning devices are able to model the anatomy of any organs. Geometric model of saccular aneurisms and of the vessel path to reach the vessel lesion with a catheter is useful (i) to point out difficult artery segments to cross with the catheter due to high tortuosity and possible atherosclerotic plaques, (ii) to choose the sites which can be used to stabilize the catheter position during coiling, (iii) to preform the catheter for easier access to the aneurism, (iv) to investigate possible compression of blood vessels by the aneurism and to plane stenting coupled to coiling and (v) to test vessel compression risk after coiling. Polygonal models of the organ surfaces are used to represent the anatomy acquired by medical imaging. The discrete surface reconstruction, the so-called facetisation, is also required for numerical simulations, which are based either on finite element or finite volume methods. Input data for the surface reconstruction of the target vessels come either from X-ray CT (Thiriet and Malandain, 1998; Cebral and Löhner, 1999, 2001), or from magnetic resonance images (Milner et al., 1998; Ladak et al., 2000), or from 3D ultrasound images (Gill et al., 2000). Besides, from input geometry only, it is not obvious to predict whether the recanalization risk is high or not. Post-treatment numerical simulations may be performed to give a better prognosis.

The present work provides (i) various available methods, among the whole set of proposed techniques, of angiography-based three-dimensional reconstructions (3DR), (ii) a single meshing method appropriate to the finite element method (FEM), whatever the 3DR, and (iii) numerical simulations of blood flows in aneurismal arteries. The investigation framework is the Cooperative Research Initiative "Vitesv", which involves mainly a set of INRIA teams working in computational geometry (PRISME Project), in image processing (EPIDAURE Project), in meshing (GAMMA Project) and fluid and solid mechanics (BANG and MACS Projects). The sequence of operations is illustrated by two different saccular wall dilatations, a side and a terminal aneurisms. The fluid domain is composed, at least, of a trunk (inward flow), a transition zone of the branching region, the branches (outward flows) and the aneurism. The facetisation is transformed into a FEM-adapted geometrical model in order (i) to ensure uniform pressure at the vessel entry and exits, (ii) to limit the disturbances induced by the boundary conditions on the flow, and (iii) to keep upstream and downstream effects of vessel geometry changes on the flow in vessel segments, which are afferent to and efferent from the explored volume. The simple best approach is to compute the flow in a compliant domain using the in vivo boundary conditions. However, in vivo velocimetry at both vessel ends is not always available in mid-size arteries due to limitation in spatial resolution of the scanning device as well as in vivo rheological properties of the artery and aneurism walls. The present work deals thus with frozen domain and boundary conditions commonly used in computational models of physiological flows.

1. Method

Blood flow simulations in aneurismal vessel of complex geometries require a set of computational tools, from the fluid domain construction to the grid generation in which numerical simulations are performed, using a computational fluid dynamics solver.

Aneurism types. Two kinds of saccular aneurisms, a cerebral aneurism (A1) and an iliac aneurism (A2), provide the geometry input data of the computational mesh, after image acquisition and processing.

Model A1. The terminal aneurism is located at the apex of the bifurcation of a branch of the middle cerebral artery (Fig. 2). Its cavity is biloculated with a very long loculus (the nose, on the left in Fig. 2). The aneurism cavity is facing the curved stem; the blood thus impacts the aneurism wall. The inlet section of the neck takes the place of both the bifurcation apex and the entrance short segment of the upper edges (with respect to the front view depicted in Fig. 2) of both terminal branches. The neck is badly defined and may be assumed to be axially short and transversally rather broad.

Model A2. The side aneurism is located at the edge of the common iliac artery, slightly upstream from a branching segment (Fig. 3). As A1, A2 presents a nose. The aneurism has a well-defined neck which appears as a narrow and short channel conveying the blood into the aneurismal cavity (the neck is narrow in the direction normal to the local vessel axis, and larger, although

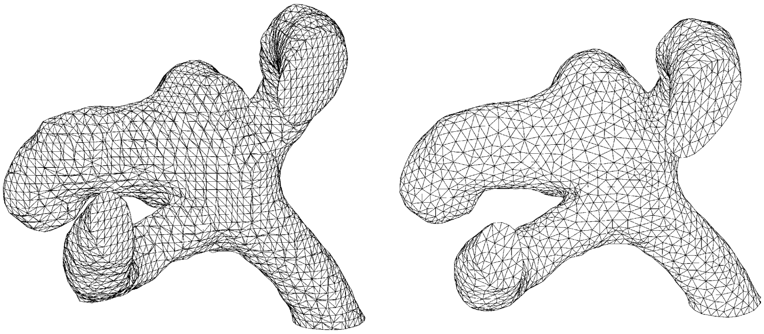

Fig. 2. Facetisation (left) and mesh (right) of the explored domain with a saccular terminal aneurism A1 (front view).

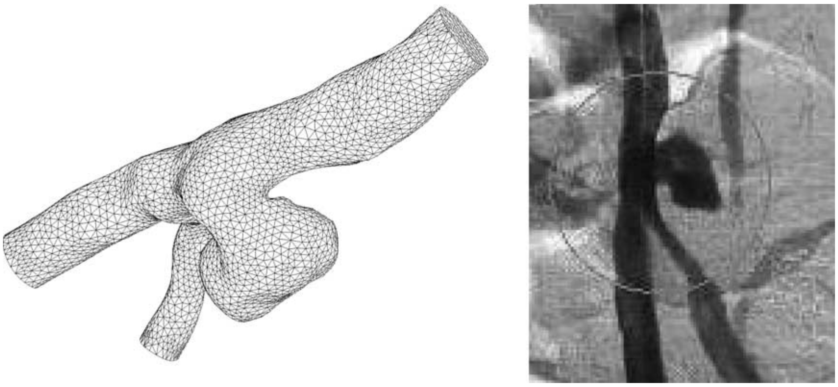

Fig. 3. Mesh of the saccular side aneurism A2M1 (left, rear view) and control RX angiography after 3D reconstruction (right).

not very wide, in the direction of the local vessel axis). Although, of relatively small size (with respect to the local vessel length scale), the iliac aneurism induces a slight compression of the branch.

1.1. Image processing and meshing

Surface meshes must match strong requirements related both to the accuracy of the surface approximation and to the element shape and size quality for the computations. Three main steps lead to the finite element mesh of the explored vessels. Angiographic images are processed to reconstruct the vessel surface, which is associated with a facetisation (step 1). A facetisation is a surface discretization which is not necessarily composed only of triangles. Morevover, the facetisation is, most often, not suitable for numerical simulations. A second stage (step 2) is thus needed in order (i) to eliminate surface artefacts (holes, interpenetrations, etc.), (ii) to simplify the surface constructed from the very large set of discrete informations to a suitable number of triangles and (ii) to ensure a computation-suited mesh, especially at vessel ends. This step provides a 3D geometrical model. During the final stage (step 3), the computational mesh is generated and adapted for fast numerical simulations of blood flow.

1.1.1. Step 1: 3D reconstruction

Medical imaging provides very large datasets of discrete data which may be very noisy. The initial surface discretization deriving from the sampled data must be simplified in order to be easily manageable. The number of triangles is reduced such that the optimal number of triangles preserves the geometry accuracy of the vessel wall of the investigated part of the vessel network.

Among the set of processing methods, various algorithms are used to reconstruct the vessel surface with its associated piecewise linear approximation. Marching-cube approaches attempt to extract an implicit surface from a 3D range image based on a ''voxelhood'' analysis (Lorensen and Cline, 1987). Delaunay tetrahedralization algorithms first generate a 3D triangulation over a point cloud and then extract a bounded surface triangulation from this set of tetrahedra using suitable topological and geometrical criteria (Boissonnat and Cazals, 2002; Amenta and Bern, 1998). Slice connection algorithms work for a series of planar parallel cross-sections. At first, a closed contour is extracted in each slice, then contours are connected to each other between each pair of adjacent slices (Boissonnat, 1988).

The 3DR of A1 uses the marching cube algorithm after image thresholding. This operation is easy because of high-quality acquired images. The marching-cube procedure introduces artefacts in the polygonal approximation (“staircases” effects). The explored domain is confined to a small region of interest, which is composed of a 3D curved trunk, the transition zone, the entrance segments of both branches and the terminal aneurism (Fig. 2). The local direction of the vessel axis is determined at each end of the vessels by a least-square method from the normal of each selected facet, which belongs to the vessel wall and have an edge on the vessel end. Short straight pipes (of length of two times the local hydraulic diameter only to avoid intersection of the branches, which is not too short when the Reynolds number is not too high and velocity boundary conditions are not applied) are added to the trunk and its bifurcation branches.

At the opposite the A2 image quality are not good and the number of saved slices is small (25% of the slice total number). But this case appears to be a good training example. The artery contours are extracted from the set of saved scan slices, with a between-slice distance of 3 mm. After noise filtering using a 2D level propagation method, a contour detection algorithm based on level set is applied (Malladi and Sethian, 1996). The vascular network of interest is composed of the downstream segment of the aorta, of its bifurcation into two common iliac arteries. The diseased common iliac artery is longer than the normal one and presents a branching segment. Three models have been derived from this network. Model A2M1 is composed of a small domain with the diseased artery, its side aneurism, the branching region and the entrance segments of both branches. The reconstruction of the 3D surface has been made using a spline-fitting method associated with a CAD software (Mossa, 2001). The 3D reconstruction is a posteriori validated by an additional angiography (Fig. 3). Models A2M2 and A2M3 correspond to the whole reconstructed network. Both are obtained using home-made softwares dedicated to surface reconstruction from polygonal contours.

The surface of A2M2 has been reconstructed from planar parallel contours using “NUAGE” software [2] (Boissonnat and Geiger, 1993). To fit up a surface on a set of contours amounts to construct a volume enclosed by these contours. The global volume is considered as the union of independent pieces resulting from pair treatment. The in-house package “Nuage” produces such a volume, dealing with one pair of consecutive contours at a time. A triangulated surface is thus drawn in between each pair of consecutive sections, ensuring that each point in a contour is connected to its closest point in the next contour. Furthermore, “Nuage” ensures, for subsequent numerical computations, the convexity of the volume delimited by two consecutive sections, when these two latters are convex. Nuage is mainly based on Delaunay triangulations and Voronoi diagrams of points located in two parallel planes (de Berg et al., 1997; Boissonnat and Yvinec, 1988).

The input points for A2M3 are also the nodes which define the vessel contours obtained by the level set method. After a cubic spline fit of each contour associated with a smoothing, a new node set is defined by equally spaced points along the vessel contour. Then, two successive slices are projected orthogonally to the local axis in a same plane and a 2D constrained Delaunay triangulation is built. The surface triangles are finally extracted by elevation of the two planes. The difference with the similar method developed by Da is that the set of intrinsic axes of the arteries give a projection direction ideal for the slice pair treatment, whereas Da uses projection direction normal to the slice planes for general purpose (Da, 2002). This adaptation to the data nature gives more suitable results for further numerical treatments. An other difference is that natural neighbour interpolation of the contours has been replaced by spline interpolation. The advantage of the technique used for A2M3 construction is that the entry and exit sections are rotated in order to be normal to the local axis. The disadvantage of this technique is to introduce high curvature branching apex, which less mimic the anatomical branching than A2M2.

1.1.2. Step 2: CFD-adapted geometrical model

The surface discretization obtained from the 3D reconstruction needs further treatment to be suitable for numerical simulations. Boundary conditions must be set sufficiently far from the exploration volume otherwise they affect the flow. Moreover, any geometry change along a vessel (bends, branching segment, lumen narrowing or enlargment, wall cavity, taper, etc.), induces flow disturbances over a given length both upstream and downstream from the causal segment. Consequently, short straight ducts in the direction of the local axis are connected to every vessel end. Furthermore, vessel-end sections must be cross-sections because of stress-free boundary conditions applied at each outlet. The blood vessel are continuously curved; curvature induces transverse pressure gradient in any bend cross-section as well as in upstream and downstream cross-sections of possible straight pipe over a given length, which depends on the values of the flow governing parameters (Thiriet et al., 1992). Besides, axial pressure gradient is exhibited in vessel section which are non-perpendicular to the vessel axis.

1.1.3. Step 3: computational mesh

The next stage consists in simplifying the initial dense surface mesh. Redundant elements are removed while preserving the accuracy of the geometric approximation of the underlying surface. The simplification procedure

---

[2] www-sop.inria.fr/prisme/logiciel/nuages.html.

is based on the Hausdorff distance. This algorithm involves vertex deletion and edge flipping. A smoothing stage based on a bi-laplacian operator is required to remove the "staircase" artefacts (Taubin, 1995). This stage yields to a geometric surface mesh that is a good approximation of the surface geometry and contains far less nodes than the initial reference mesh (Frey and Borouchaki, 1998). Surface smoothing and triangle-number optimisation (the triangulation is coarsened in the regions where the local curvatures are sufficiently large, whereas the main local curvatures are kept; the mesh is enriched in sharp regions with possible flow complex behaviour) is done using the different abilities of "YAMS" software (Frey, 2001).

As numerical simulations are the final objective of our study, element shapes and sizes must be controlled as they usually impact the accuracy of the numerical results (Ciarlet, 1978). Therefore, an anisotropic geometric metric map based on the local principal directions and radii of curvatures is constructed in the tangent planes related to the mesh vertices. This metric map prescribes element sizes proportional to the local curvature of the surface (Frey and Borouchaki, 2003). The metric map can also be combined with a computational metric map (e.g., supplied by an a posteriori error estimate) and eventually modified to account for a desired mesh gradation. Then, a surface mesh generation algorithm is governed by the metric map and based on local topological and geometrical mesh modifications. This approach can be easily extended to mesh adaptivity as it involves metrics to generate the mesh.

The conforming surface triangulation must be topologically accurate to generate a volumic mesh. The last step provides a tetrahedral mesh, using the fully automatic tetrahedral mesh generator "GHS3D" [3] (George, 1997). The numbers of points and elements for the computational meshes are given in Table 1.

1.2. Flow computations

1.2.1. Governing equations

The blood, concentrated suspension of cells, is supposed to be incompressible, homogeneous and Newtonian, because red blood cells (RBC) are assumed neither to have time enough to aggregate (the time constant of RBC aggregation is supposed to be greater than the convective time scale) nor to deform in the large blood vessels.

The governing equations of a vessel flow are derived from the mass and momentum conservation

$$\nabla \cdot \mathbf{u} = 0; \quad \rho(\mathbf{u}_t + (\mathbf{u} \cdot \nabla)\mathbf{u}) = \mathbf{f} + \nabla \cdot \mathbf{C},$$

where $\mathbf{u}$ is the fluid velocity (subscript t: time derivative), $\mathbf{f} = -\nabla\Phi$ the body force density (Φ: potential from which body force per unit volume are derived), $\mathbf{C} = -p_i\mathbf{I} + \mathbf{T}$ the stress tensor, $\mathbf{T} = 2\mu\mathbf{D}$ the extra-stress tensor (Newtonian fluid), $\mathbf{D} = (\nabla\mathbf{u} + \nabla\mathbf{u}^{\mathrm{T}})/2$ the deformation rate tensor, $\mathbf{I}$ the identity tensor, ρ the fluid density and μ the fluid dynamic viscosity. With the given fluid properties, the Navier–Stokes equation becomes

$$\rho(\mathbf{u}_t + (\mathbf{u} \cdot \nabla)\mathbf{u}) = -\nabla p_i^* + \mu\Delta\mathbf{u}, \tag{1}$$

where $p_i^* = p_i + \Phi$. The pressure notation is simplified in the following sections ($p_i^* = p$).

The dimensionless governing equations

$$St\tilde{\mathbf{u}}_{\tilde{t}} + (\tilde{\mathbf{u}} \cdot \widetilde{\nabla})\tilde{\mathbf{u}} - Re^{-1}\widetilde{\Delta}\tilde{\mathbf{u}} + \widetilde{\nabla}\tilde{p} = 0; \quad \widetilde{\nabla} \cdot \tilde{\mathbf{u}} = 0 \tag{2}$$

are obtained when dimensionless quantities are given by $\tilde{t} = t/T^{\star}$, $\tilde{x} = x/L^{\star}$, $\tilde{u} = u/U^{\star}$, $\tilde{p} = p/(\rho U^{\star 2})$, and where St and Re are the Strouhal- and the Reynolds number respectively. With the unity scales usually taken in numerical analysis, the dimensionless governing equations become

$$\tilde{\mathbf{u}}_{\tilde{t}} + (\tilde{\mathbf{u}} \cdot \widetilde{\nabla})\tilde{\mathbf{u}} = -\widetilde{\nabla}\tilde{p} + \nu\widetilde{\Delta}\tilde{\mathbf{u}}; \quad \widetilde{\nabla} \cdot \tilde{\mathbf{u}} = 0. \tag{3}$$

The vessel wall is assumed to be rigid. The boundary of the fluid domain is partitioned into a surface set: the entry Γ_1, the exit cross-sections Γ_2 and the pipe wall Γ_3. The classical no-slip condition is applied to the vessel wall. A time-dependent uniform injection velocity is prescribed at the inlet, after applying a Fourier transform on the data set derived from in vivo MR velocimetry. At the outlet cross-sections, normal constraint is equal to zero.

The stem peak Reynolds number based on the peak cross-sectional average velocity and on the trunk radius at the entrance cross-section is equal to about 160 in A1 and about 1110 in A2. The Stokes number (frequency parameter), based on the trunk radius at the entrance cross-section and the Strouhal number are equal to 1.6 and 0.02 in A1 and to 11.2 and 0.11 in A2, respectively.

1.2.2. Numerical simulations

The numerical technique to solve the classical fluid mechanics equations for incompressible fluids is the finite element method (Hecht and Pares, 1991). It is based on a variational formulation of the Navier–Stokes equations on a domain Ω

$$\mathscr{B}(\mathbf{u},\mathbf{v}) + \mathscr{T}(\mathbf{u};\mathbf{u},\mathbf{v}) + \mathscr{B}'(\mathbf{v},p) = \langle l,\mathbf{v}\rangle$$
$$\forall\mathbf{v} \in V \subset H^1(\Omega)^3,$$

$$\mathscr{B}'(\mathbf{u},q) = 0 \quad \forall q \in Q \subset L^2(\Omega),$$

where $\mathscr{B}$ and $\mathscr{B}'$ are bilinear forms, $\mathscr{T}$ a trilinear form, $\langle l,\mathbf{v}\rangle$ the dual product (the quantity l takes into account the nonhomogeneous velocity and possible pressure boundary conditions as well as the possible forcing term $\mathbf{f}$), $H^1(\Omega)$ and $L^2(\Omega)$ the Sobolev space of order 1 defined

---

[3] www-rocq.inria.fr/gamma/ghs3d/ghs.html (TetMesh, distributed by SIMULOG, www.simulog.fr/tetmesh/).

Table 1
Aneurism mesh features

	A1	A2M1	A2M2	A2M3
Node number	7910	12800	10820	12550
Element number	36970	63360	50270	58250

on Ω for vector-valued functions and the space of functions that are square integrable in the Lesbegue sense with respect to Ω, respectively.

The computational method is suitable to unsteady flow, the time being used as an iterative parameter of the solution. The finite element type is P_1–P_1 bubble element for pressure and velocity approximation respectively (Arnold et al., 1984). The convective term is approximated by the method of characteristics (Pironneau, 1982). The solution is obtained via a generalized Uzawa-preconditioned-conjugate gradient method (Glowinski, 1984). The initial condition is given by a Stokes problem with the same boundary condition as the unsteady one (period of 1 s).

2. Results and discussion

2.1. A2 computational domains

The meshing techniques, with their respective advantages and drawbacks, have been used to investigate the reconstruction quality and its repercussion on the flow field. The aorta-apex design is better in A2M2 but the vessel configuration is much less smooth than in A2M3. The shape of both the aneurism sac and neck is also highly dependent on the 3D reconstruction procedure (Fig. 4). In A2M1, the nucha edge exhibits a slight vertex, like in the control angiography (Fig. 3), while it is rather flat in both A2M2 and A2M3. The nose front edge of A2M2 is flat with angular ends between the top and bottom edges. It is also flat in A2M3, but with curved ends as the edge shape displayed in the control angiography. The nose front edge of A2M1 is curved with a top facing the nucha edge vertex. The dome of A2M1 is longer than in the two other models. The neck is narrower in A2M1 than in A2M2 whereas it is wider in A2M3 than in A2M2. The relative ratio between the neck width and the sac width of the A2 models with respect to the ratio measured in the control angiography (Fig. 3) is equal to about 0.73, 1.07 and 1.39 in A2M1, A2M2 and A2M3 respectively. It is thus closer in A2M2 to the measured value. The aneurism height-to-width ratio is approximately equal to 0.82, 1.01, 0.98 in A2M1, A2M2 and A2M3, respectively, whereas it is equal to ~0.75 in the control angiography. This geometry index is then better determined by the reconstruction procedure used in A2M1.

2.2. Numerical results

Velocity profiles plotted at given cycle phases from arbitrary lines of selected aneurism planes for five successive cardiac cycles shows that the initialization procedure

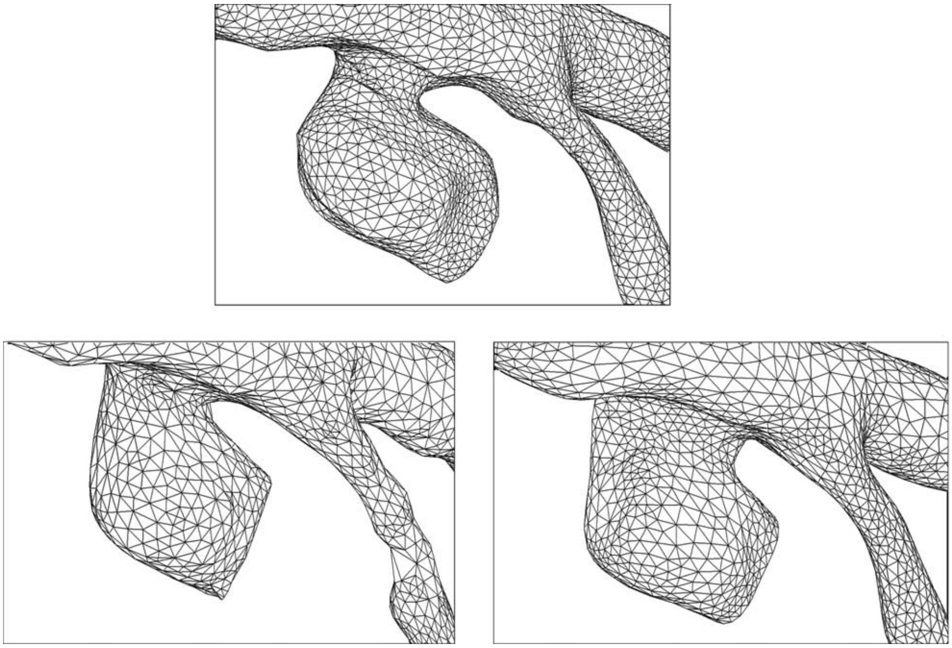

Fig. 4. Zoom on the A2 meshes. Model A2M1 (top), A2M2 (bottom, left), A2M3 (bottom, right).

does not disturb significantly the results. The velocity profiles are wholly superimposed from the second period cycle. Due to slight differences in the velocity magnitude at given spaces and cycle phases between the two first periods, the first period can be considered to give a representative flow. Such a result can be explained by computation initialization using a Stokes problem rather than other initial conditions, as potential flows. The effect of the Stokes initialization mode is thus quickly damped during the unsteady computation.

Streamlines and velocity vector plots at different phases of the cardiac cycle show that, due to the aneurism implantation, the blood runs widely through A1, whatever the cycle phase, while blood streams at peak flow in A2. The pressure field is assumed to be the major factor of aneurism plastic deformation. Measurements cannot be done in vivo without great disturbances. Only few pressure stations can be set in physical models of the artery lesions. At the opposite, numerical tests provides the pressure field with a very good spatial resolution. Few phases of the cardiac cycle are selected in order to plot the pressure fields: (i) phase 1 at about 2/3 of the time duration of the accelerating phase, (ii) phase 2 slightly after peak flow, (iii) phase 3 at the beginning of the decelerating phase when the instantaneous flow rate is nearly the same as in phase 1, and (iv) phase 4 at about 3/4 of the time duration of the decelerating phase.

In the terminal aneurism, the pressure reaches higher values than in the side aneurism, in agreement with the blood motion. Two main regions of high pressure are observed in A1 throughout the cardiac cycle (Fig. 5). The first region appears at the dome part facing the neck and the second one at the front face of the neck. The size of high pressure zones varies during the flow cycle. These two regions merge at peak flow and during the beginning of the decelerating phase. The pressure in these regions rises during the same cycle phases with a relative difference of about 6%. A third high-pressure region occurs at the nose end at peak flow and quickly disappears during the decelerating phase. The wall of A1 dome and front face are impacted by the blood flowing from the trunk core region throughout the cycle with more or less strong magnitude. The high-pressure zone in the neck gives an argument in favour of the surgical clipping because the aneurism is superficial with an easy surgical access. It is not possible, indeed, to protect efficiently the neck with coiling because coils in this location will always induce emboli. However, if the endovascular treatment is chosen with respect to heav-

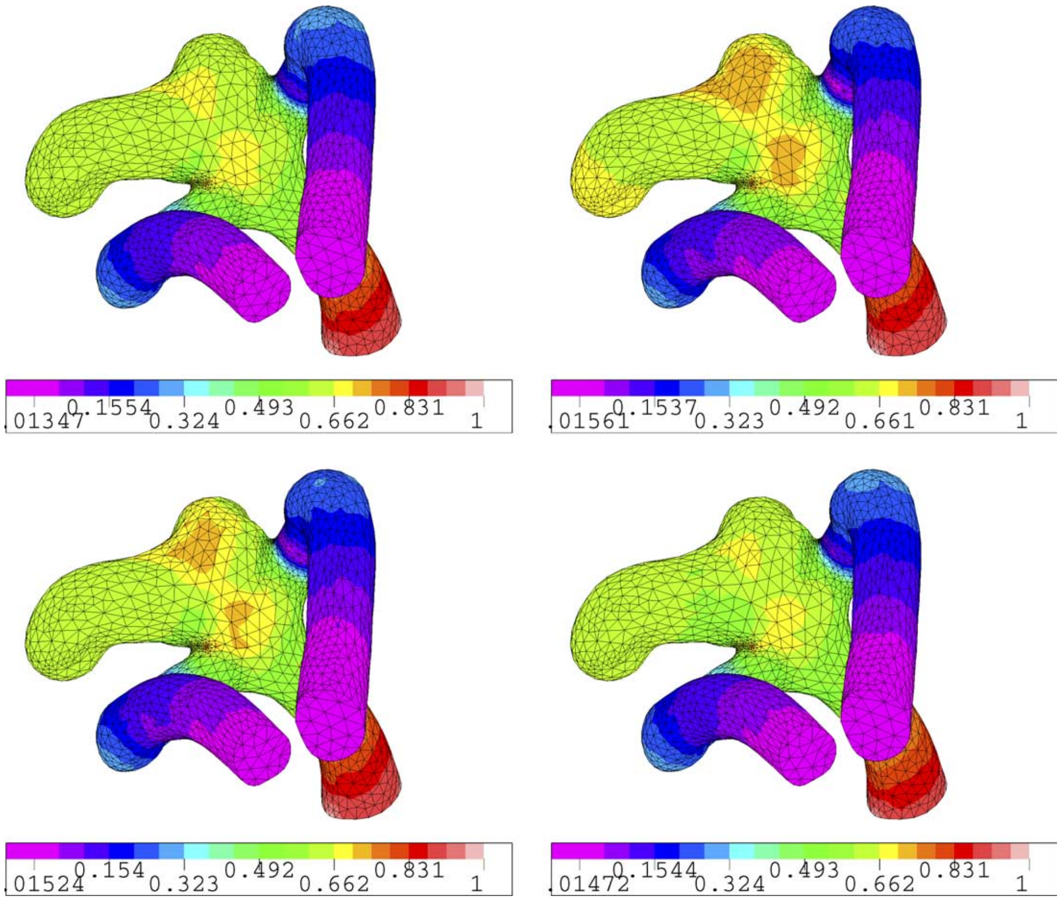

Fig. 5. Pressure field in the A1 model at the four selected phases of the cardiac cycle. Front view.

ily-invasive surgery, frequent angiography control must be made because of high risk of recanalization.

The pressure in the side aneurism remains lower than in A1 throughout the cardiac cycle (Fig. 6). The amount of blood flowing into A2, mainly at peak flow, is much lower than in A1. Moreover, the blood does not impact directly the aneurism wall. Although the rupture risk is not very high, an appropriate treatment may be done because of the slight associated compression of the artery branch. Due to A2 implantation and its neck configuration, coiling is easier than in A1. The size of the explored vascular region is expected to affect the pressure within the aneurism. However, the relative difference in normalized pressure maximum between A2M1 and A2M3, characterised by a smoother vessel configuration than A2M2, is nearly equal to 5%. On the contrary, the configuration of the computational domain, which model the same region of the vessel network, affects the field of the haemodynamic quantities (Fig. 7). The aneurism pressure is smaller in A2M3 than in A2M2 (relative difference in pressure maximum of about 25%).

The greater the mesh element density, the better the quality of the results (governing equations are founded by the continuum concept), but the longer the computational time required for time-dependent flow simulations. The highest difference in the flow-quantity fields has been found to be equal to about 16% when the A1 mesh is refined (element number is multiplied by approximately four). The mesh-element number affects similarly the numerical results than the 3D reconstruction. Such differences between the fields of flow quantities, although significant, remain reasonable in the context of sequential multimodeling involved from image processing to 3DR and meshing and, last, to numerical simulations. In order to quickly get results, the mesh-element number is fixed to the lower admissible value to ensure correct domain shapes and finite element meshes. In the present work, only available techniques of 3D reconstruction of vessel segments were used. Markov random field models have also been successfully introduced in image analysis (Descombes et al., 1999), as well as deformable models (Delingette et al., 1992). In any case, the results depends on the image quality. Furthermore, the numerical models usually assumed rigid vessel walls. The artery wall is deformable but the influence of the wall motion on the flow field must still be determined. Although a robust blood-wall interaction software is available and has been recently tested with A1 (Gerbeau and Vidrascu, 2003), one needs suitable in vivo rheological data on human vessel wall, which may differ greatly from in vitro parameters. Another model limitation is given by the crude boundary conditions set at the vessel exits. Multiscale modeling is necessary because the region of interest is a part of the circulatory network with its upstream and downstream properties, which ensures the physiological flow behaviour. Besides, multiphysics models must be coupled to multiscale models of the blood vessels in order to avoid wave reflection artefacts.

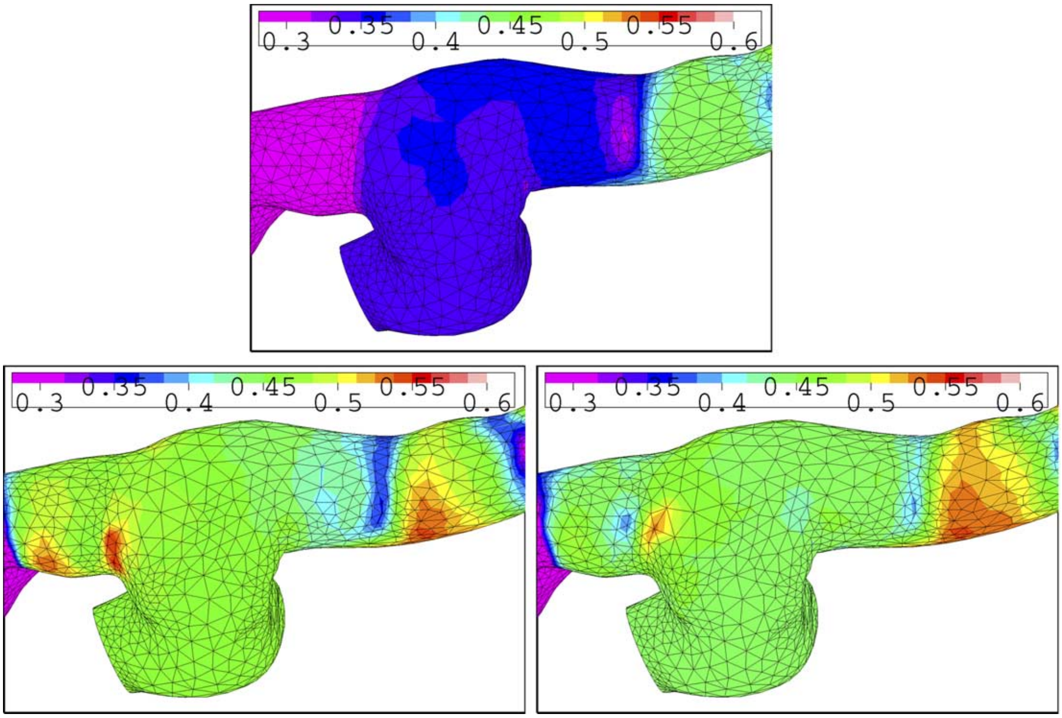

Fig. 6. Pressure field in A2M3 at selected phases 1, 2 and 4 of the cardiac cycle. Same range of the normalized pressure $p_+ = \tilde{p}/\tilde{p}_{\max} \in [0.3, 0.6]$ for the three phases. Zoom on the aneurism.

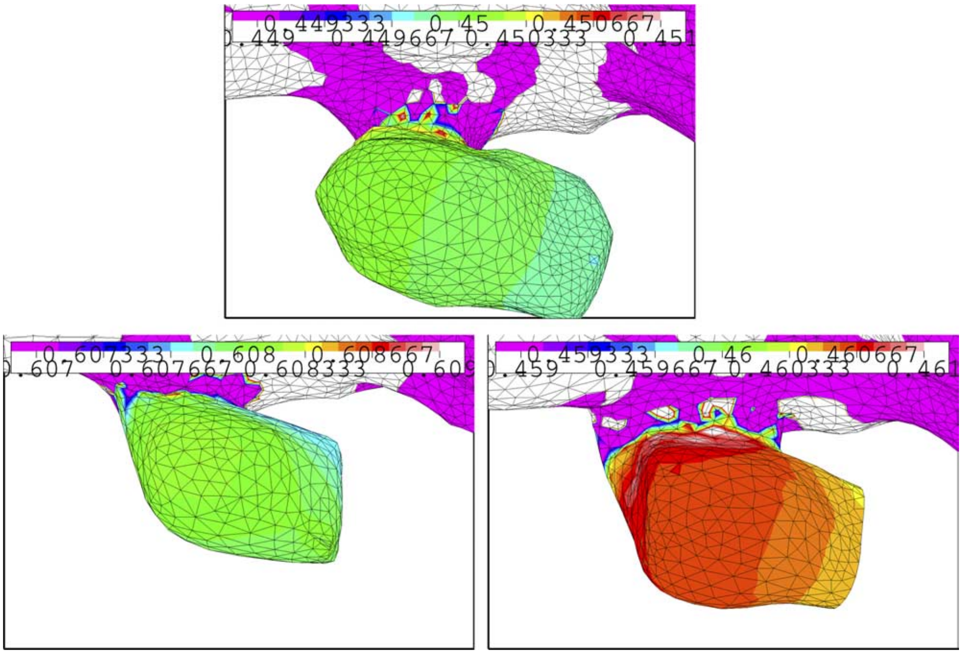

Fig. 7. Pressure field in A2 model at peak flow. Zoom on the aneurism. A2M1 (top, $p_+ = \tilde{p}/\tilde{p}_{\max} \in [0.449, 0.451]$), A2M2 (bottom, left, $p_+ \in [0.607, 0.609]$) and A2M3 (bottom, right, $p_+ \in [0.459, 0.461]$).

3. Conclusion

The present work is mainly performed in the context of mini-invasive treatments of artery wall diseases, characterized by catheter-based implantation of medical devices. Saccular aneurisms are here taken as examples of wall lesions. Peroperative risks, as rupture and thrombo-embolism, stimulate the development of computer-aided treatments. Such tools must (i) provide a visualisation of the diseased region and its surroundings, (ii) give a planification tool in order to optimize the treatment and to minimize the risk of peroperative complications and (iii) forecast the effects of the treatment on the local blood flow and project the short term evolution of the treated vessels. Navigation tools for endoluminal catheter displacement and device installation control, as well as augmented reality training simulator for a pretherapeutic preparation of the travel and deployment of the catheter-based medical device, are also demanded by interventional physicians. In any case, the stage of geometrical modeling is crucial.

The marching-cube technique fastly provides geometrical models but needs a complete set of high-quality images. In case of poor-quality images and partially saved slices, slice connection methods are fruitful. Images provided with a poor resolution and partially saved lead to different vessel configurations and numerical results which, although significant, is reasonable in the multimodeling process. Differences in values of the flow variables are also observed when the mesh is refined. These quantitative differences are not associated with any change in the flow pattern, the main flow properties remaining similar. However, new techniques, more suitable to the blood vessels, are in development, based on vessel axis determination and non-linear multi-scale contour detection (Krissian et al., 1998; Matei, 2002). Such techniques allow to define quickly vessel cross-sections, but also to extract a vessel network almost topologically perfect.

High pressure zones are observed, especially in terminal aneurisms. The greater the pressure, the higher the risk of aneurism rupture. In the case of aneurisms, an additional question arises. Where is the site of within-wall high-stress concentration, susceptible to rupture? Is it spatially correlated with the within-cavity high-pressure region?

Acknowledgements

Support for this work was provided by INRIA with ARC VITESV. The authors thank F. Nicoud who provides the set of A2 contours.

References

Amenta, N., Bern, M., 1998. Surface reconsruction by Voronoi filtering. In: Proc. 14th Annu. ACM Symp. Comput. Geom., Minneapolis, pp. 39–48.

Arnold, D.N., Brezzi, F., Fortin, M., 1984. A stable finite element for the Stokes equations. Calcolo 21, 337–344.

de Berg, M., van Kreveld, M., Overmars, M., Schwarzkopf, O., 1997. Computational Geometry: Algorithms and Applications. Springer-Verlag, Berlin.

Boissonnat, J.D., 1988. Shape reconstruction from planar cross-sections. Comput. Vision Graph. Image Process. 44, 1–29.

Boissonnat, J-D., Geiger, B., 1993. Three dimensional reconstruction of complex shapes based on the Delaunay triangulation. In: Acharya, R.S., Goldgof, D.B. (Eds.), Biomedical Image Processing and Biomedical Visualization, SPIE, 1905, Int. Soc. Opt. Eng., Bellingham, WA, pp. 964–975.

Boissonnat, J-D., Yvinec, M., 1988. Algorithmic Geometry. Cambridge University Press, UK.

Boissonnat, J.D., Cazals, F., 2002. Smooth surface reconstruction via natural neighbour interpolation of distance functions. Comp. Geom. 22, 185–203.

Cebral, J.R., Löhner, R., 1999. From medical images to CFD meshes. Proc. Int. Meshing Roundtable, 321–331.

Cebral, J.R., Löhner, R., 2001. From medical images to anatomically accurate finite element grids. Int. J. Numer. Meth. Eng. 51, 985–1008.

Ciarlet, P.G., 1978. The finite element method for elliptic problems, Studies in Mathematics and its Applications, 4, North-Holland, Amsterdam.

Da, T.K.F., 2002. L'interpolation de formes, Ph.D. Thesis, Nice University.

Delingette, H., Hébert, M., Ikeuchi, K., 1992. Shape representation and image segmentation using deformable surfaces. Image Vision Comput. 10 (3), 132–144.

Descombes, X., Sigelle, M., Prêteux, F., 1999. Estimating Gaussian Markov random field parameters in a nonstationary framework: application to remote sensing imaging. IEEE Trans. Image Process. 8 (4), 490–503.

Frey, P.J., 2001. A fully automatic adaptive isotropic surface remeshing procedure. INRIA Research Report, 0252.

Frey, P.J., Borouchaki, H., 1998. Geometric surface mesh optimization. Comput. Visual. Sci. 1, 113–121.

Frey, P.J., Borouchaki, H., 2003. Surface meshing using a geometric error estimate. Int. J. Numer. Meth. Eng., to appear.

George, P.L., 1997. Improvement on Delaunay based 3D automatic mesh generator. Finite Elem. Anal. Des. 25 (3–4), 297–317.

Gerbeau, J.-F., Vidrascu, M., 2003. A Quasi-Newton algorithm based on a reduced model for fluid-structure interaction problems in blood flows. Math. Modell. Numer. Anal. M2AN 37 (4), 663–680.

Gill, J.D., Ladak, H.M., Steinman, D.A., Fenster, A., 2000. Accuracy and variability assessment of a semi-automatic technique for segmentation of the carotid arteries from 3D ultrasound images. Med. Phys. 27, 1333–1342.

Glowinski, R., 1984. Numerical methods for nonlinear variational problems. Springer Series in Computational Physics. Springer-Verlag, Berlin.

Hecht, F., Pares, C., 1991. NSP1B3: un logiciel pour résoudre les équations de Navier Stokes incompressible 3D, INRIA Research Report, 1449.

Krissian, K., Malandain, G., Ayache, N., 1998. Model based multiscale detection and reconstruction of 3D vessels, INRIA Research Report, 3442.

Ladak, H.M., Milner, J.S., Steinman, D.A., 2000. Rapid 3D segmentation of the carotid bifurcation from serial MR images. ASME J. Biomech. Eng. 122, 96–99.

Lorensen, W.E., Cline, H.E., 1987. Marching cubes: A high resolution 3D surface construction algorithm. Comp. Graph. 21 (4), 163–169.

Malladi, R., Sethian, J.A., 1996. Image processing: flows under min/max curvature and mean curvature. Graph. Model Image Process. 58, 127–141.

Matei, B., 2002. Méthodes multiéchelles non-linéaires et applications au traitement d'images. Thèse de l'université Pierre et Marie Curie, Paris.

Milner, J.S., Moore, J.A., Rutt, B.K., Steinman, D.A., 1998. Hemodynamics of human carotid artery bifurcations: computational studies with models reconstructed from magnetic resonance imaging of normal subjects. J. Vasc. Surg., 143–156.

Mossa, J.B., 2001. Simulation d'une bifurcation artérielle, CERFACS Report.

Pironneau, O., 1982. On the transport–diffusion algorithm and its application to the Navier–Stokes equations. Numerische Mathematik 38, 309–332.

Taubin, G., 1995. Curve and surface smoothing without shrinkage. 5th Int. Conf. Comp. Vision Proc., 852–857.

Thiriet, M., Issa, R., Graham, J.M.R., 1992. A pulsatile developing flow in a bend. J. Phys. III, 995–1013.

Thiriet, M., Malandain, G., 1998. Modélisation numérique de l'écoulement dans les anévrismes cérébraux. Arch. Physiol. Biochem. 106, 108.